JOURNAL OF THE ROYAL SOCIETY Interface

J. R. Soc. Interface (2009) **6**, 519–528
doi:10.1098/rsif.2008.0417
Published online 25 November 2008

Arterial geometry, flow pattern, wall shear and mass transport: potential physiological significance

G. Coppola* and C. Caro

Department of Bioengineering, Imperial College, London SW7 2AZ, UK

We have studied numerically steady and unsteady flow in a straight and a helically stented common carotid artery, in order to model porcine experimental results that show reduced intimal hyperplasia (IH) in the helical case. The combination of flow pulsatility and three-dimensionality generates a sweeping motion of the Dean vortices, which overall reduced extremes of both oxygen flux to the vessel wall and wall shear stress (WSS). Since IH and atherosclerosis affect preferentially low WSS regions, these findings imply that vessel three-dimensionality and flow pulsatility can play important protective roles in respect of these diseases. The amplitude and frequency of the velocity waveform are important parameters of the system. Increase in amplitude increases WSS and oxygen flux to the vessel wall. Increase in frequency has a small effect; it increases WSS but has no effect on the oxygen flux to the vessel wall.

Keywords: endovascular stent; carotid artery; flow waveform; pulsatile flow; mass transport; wall shear stress

1. INTRODUCTION

It is widely accepted that the local flow field in arteries strongly influences their biology and development of pathology (Davies 1995; Gimbrone 1999; Malek *et al.* 1999). In particular, atherosclerosis occurs preferentially where wall shear stress (WSS) is low and there is flow stagnation (Caro *et al.* 1971; Davies 1995; Giddens 1995; Gimbrone 1999; Malek *et al.* 1999). It is also widely accepted that arterial geometry is commonly three-dimensional, or non-planar, with significant effects on the local flow field (Caro *et al.* 1996). *In vivo* and model studies in idealized and realistic non-planar geometries show strong secondary motion, in-plane mixing, a relatively uniform distribution of wall shear, and suppression of flow separation, flow instability and flow stagnation (Caro *et al.* 1998, 2006; Wood *et al.* 2006). They show, moreover, that, compared with planar geometry, there can be secondary-motion-enhanced flux of low molecular weight species between the blood and vessel walls (Tarbell 2003; Caro *et al.* 2006; Coppola & Caro 2008).

Endovascular stents are widely used, but a major problem associated with their use is restenosis. This is primarily caused by the development of intimal hyperplasia (IH), typically within or downstream of the stent. The main prevailing explanation for stent-related IH is that it results from mechanical injury to the vessel, inflicted by implantation of the device. The stent restenosis problem is being addressed by a variety of measures, including drug elution. However, the cost of drug-eluting stents exceeds that of conventional stents and problems have emerged with their use. The patency of drug-eluting stented femoral arteries was not superior to that of bare metal stented vessels at 24 months, when the drug can be presumed to have been eluted (Duda *et al.* 2006). In addition, there were with drug-eluting stents inhibition of in-stent healing and instances of late stent thrombosis in coronary arteries, leading to sudden death (Nakazawa *et al.* 2007).

IH is also the principal cause of failure of arteriovenous vascular access grafts and arterial bypass grafts; it appears to develop preferentially in regions of such grafts characterized by low or oscillatory WSS (Sottiurai *et al.* 1989; Bassiouny *et al.* 1992) and hypoxia (Lee *et al.* 2000). Interestingly, it is reported that IH can be reversed by enhanced oxygen supply (Lee *et al.* 2001).

A self-expanding small amplitude helical (SMAHT) stent (Shinke *et al.* 2007) has been developed, which causes the centreline of the vessel in which it is implanted to follow a helical path. As a consequence, mixing is promoted within and downstream of the stent section, which could be expected, through geometry-induced secondary flows, to modify the distribution of WSS (Coppola & Caro 2008) and enhance oxygen supply to the vessel walls. In a recent pilot study (Shinke *et al.* 2007), two pigs were implanted with

---

*Author for correspondence (g.coppola@imperial.ac.uk).

Electronic supplementary material is available at http://dx.doi.org/10.1098/rsif.2008.0417 or via http://journals.royalsociety.org.

Received 25 September 2008
Accepted 4 November 2008

This journal is © 2008 The Royal Society

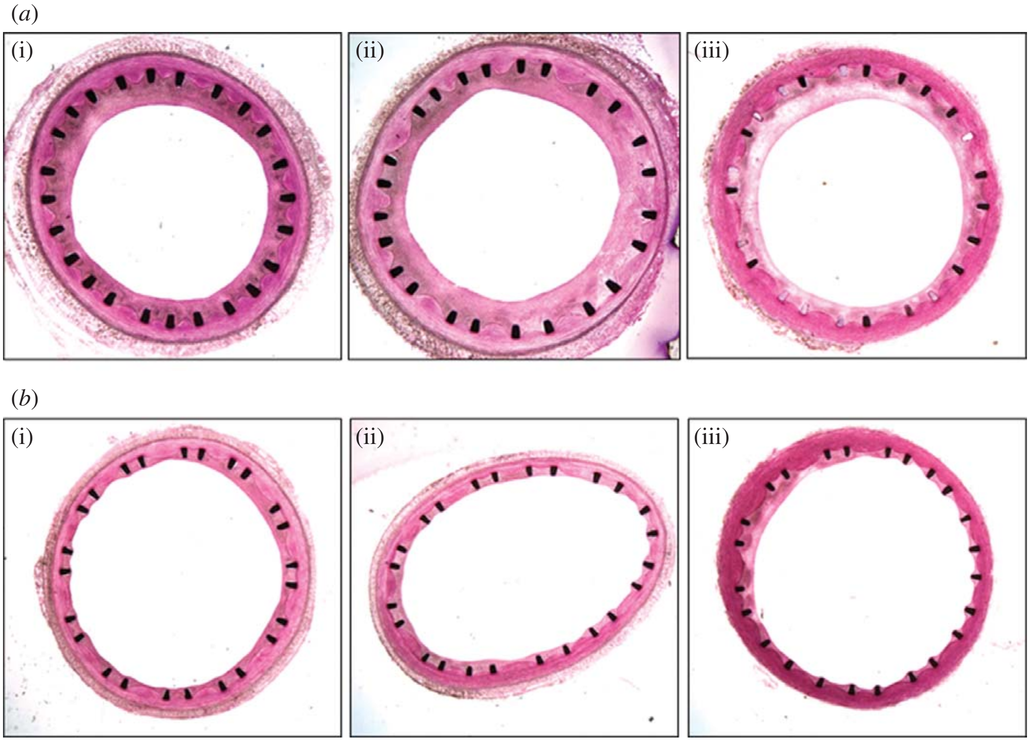

Figure 1. Histology of stented common carotid arteries ((*a*) straight stent, (*b*) helical stent) at one month post-implantation ((i) proximal, (ii) middle, (iii) distal). Reproduced with permission from Shinke *et al.* (2007). Copyright © Veryan Medical Limited.

a conventional stent in one common carotid artery (CCA) and a helical stent in the contralateral artery, and the animals were euthanized one month post-implantation. The stented carotid segments were embedded in methyl methacrylate and transverse histological sections were prepared, using a precision saw-and-grinding method (figure 1). The extent of IH in the helical stent was far less than that in the conventional one, consistent with the changes brought about by the helical geometry, including higher oxygen transport rates and WSS levels (Coppola & Caro 2008) limiting the development of IH. Interestingly, as also reported previously, sections of the helical stent showed a region of thin neointima approximately opposed to a region where the struts were covered by a thicker neointima. These two regions were rotated about the centre by some angle, which suggests that their spatial distribution along the stent was possibly helical.

Stimulated by these findings (a larger trial in 10 pigs giving confirmatory results has been reported (Shinke *et al.* 2008)), we have investigated numerically the influence of the local flow field on both the supply of oxygen to the arterial wall and the distribution of WSS, in idealized representations of the CCA, stented with a straight and a helical stent. There has been extensive study of pulsatile flow in arteries (Nichols & O'Rourke 1990; Davies *et al.* 2007) but relatively little investigation of the interaction between these phenomena and the biology of vessels and their development of disease. The investigation has therefore been performed with both steady and pulsatile flow, including an examination of the possible influence of frequency and amplitude.

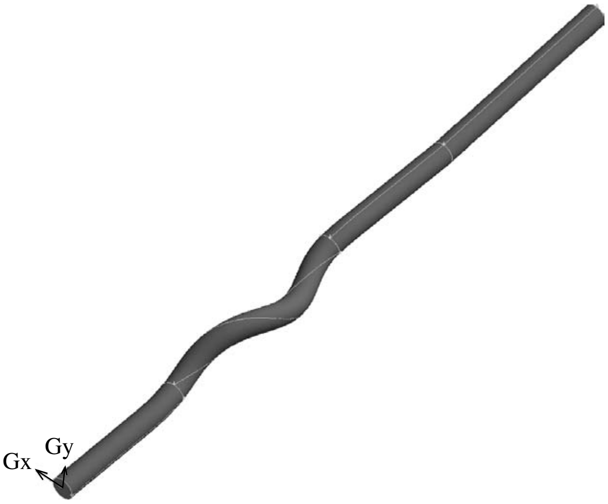

Figure 2. Computational model.

2. METHODS

2.1. Computational domain and model

The computational domain (figure 2) is represented by a CAD-generated idealized representation of the stented pigs' CCA. The stent struts are assumed to have negligible thickness and the surrounding vessel is assumed to have the shape imposed by the stent. The first assumption may not be fully justified immediately after implant, but it is a reasonable assumption after some time (figure 1). The second assumption is justified by experimental observations (figure 3).

The internal diameter of the vessel $D_i = 6$ mm and the geometry has been extended by cylindrical sections placed upstream (approx. $6.5D_i$ long) and downstream

Figure 3. Carotid/stent shape one month post-implantation. Reproduced with permission from Shinke *et al.* (2007). Copyright © Veryan Medical Limited.

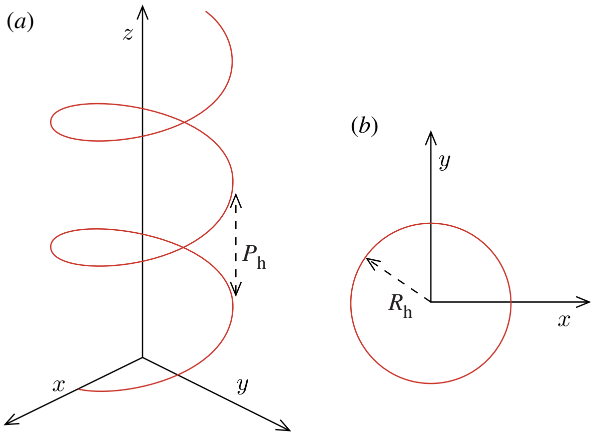

Figure 4. Definition of (*a*) helix pitch, P_h, and (*b*) helix radius, R_h.

(approx. $16D_i$ long) of the stent, to guarantee domain-independent solutions. The helical section is defined by the helix pitch, $P_h = 8D_i$, and radius, $R_h = 0.5D_i$ (figure 4) and extends for a length $L \sim 9.5D_i$. The commercial code FLUENT v. 6.0 (Fluent Inc.) was used to solve the three-dimensional steady/unsteady incompressible Navier–Stokes equations for the flow and the three-dimensional steady/unsteady advection–diffusion equation for the mass transport. The equations were discretized on a structured set of finite volumes. The SIMPLE formulation (Patankar & Spalding 1972) was used for pressure–velocity coupling, and the second-order upwind discretization scheme was used for the momentum and species transport equations. Convergence was achieved when the maximum mass, momentum and species residuals fell below 10^{-9} in the steady case, and 10^{-5}, each time step, in the unsteady case.

Newtonian behaviour was assumed for the blood, with density $\rho = 1050\ \mathrm{kg\ m^{-3}}$ and viscosity $\mu = 0.0035\ \mathrm{kg\ m^{-1}\ s}$. Oxygen was assumed to be present only in dissolved form in the plasma (Qiu & Tarbell 2000; Ethier 2002; Perktold *et al.* 2002; Coppola & Caro 2008), with diffusivity $D_{O_2} = 1.2 \times 10^{-9}\ \mathrm{m^2\ s}$, giving a Schmidt number $Sc = \nu / D_{O_2} \sim 2800$.

Fully developed flow and uniform inlet oxygen mass fraction, $y_i = 0.002125$, were imposed at the inlet. At the outflow, a stress-free condition was assumed for the flow and zero flux condition for the species. No-slip conditions for the flow and fixed oxygen concentration, $y_w = 0.0015$, were assumed at the walls for simplicity (Tarbell 2003; Coppola & Caro 2008). While this is a first-order approximation, equivalent to decoupling the wall side from the blood side mass transfer, it will not affect qualitatively the distribution of oxygen flux to the walls, although it may affect the absolute values. Nevertheless, since the purpose of this work is to compare two models in relative terms, we believe that our conclusions will not be altered by this approximation. For comparison with the experimental data, represented by slices taken at the proximal, middle and distal ends of the stent, all the results are presented at sections taken at axial locations, $z = 45$ mm (approx. 4.5 mm downstream of the stent entry section), $z = 69$ mm (half-way through the stent) and 92 mm (approx. 5.5 mm upstream of the stent end section), representative of the proximal, medial and distal sections of figure 1. To describe the behaviour of the wall-related quantities, a local polar coordinate system (r, θ) has been adopted, with its origin coincident with the centre of each section and the $\theta = 0$ line corresponding to the horizontal ($\theta > 0$ counterclockwise). The mass transport boundary layer was resolved by placing the first three grid nodes at approximately 7.6, 9 and 10.8 μm away from the wall. The results were checked for grid independence by running steady simulations at the peak *Re* number, on three grids with increasing number of elements, 325 008, 628 383 and 1 299 030. Convergence was assessed on the WSS and non-dimensional oxygen flux profiles around the sections at $z = 45$, 69 and 92 mm (figure 5). The WSS profiles are almost indistinguishable for the two most refined grids, with the largest difference of approximately 3 per cent at $z = 69$ mm. The difference in the *Sh* profiles is more relevant, reaching approximately 17 and approximately 43 per cent at the minima, respectively, at $z = 92$ and 69 mm, for the two most refined meshes. This relatively large error does not alter the qualitative behaviour of the quantity of interest and will not affect our conclusions, and given the high computational load and storage requirements demanded by the most refined mesh, all the simulations were performed with the intermediate mesh (628 383 elements). The results are presented in terms of oxygen mass fraction, helicity, WSS and *Sh*. Helicity is defined as the dot product of vorticity and the velocity vectors and is used to underline vortex structures. *Sh* is defined as the concentration gradient normal to the wall normalized by the concentration difference between the inlet and the wall divided by the vessel diameter:

$$Sh = \frac{-\frac{\partial y}{\partial n} D_i}{y_i - y_w},$$

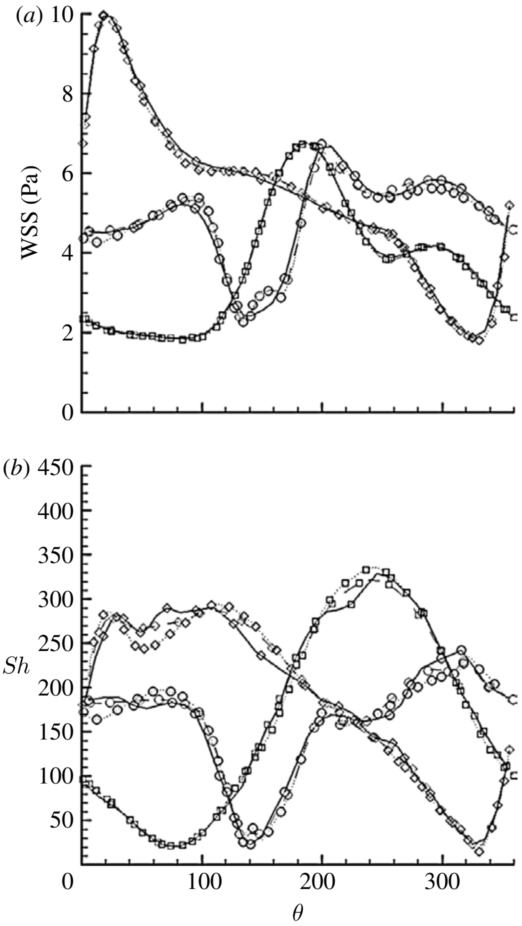

Figure 5. (*a*) WSS and (*b*) *Sh* steady-state distributions along the circumference of the cross sections at different axial locations. Squares, $z=45$ mm; diamonds, $z=69$ mm; circles, $z=92$ mm; solid lines, 325 008 elements; dashed lines, 628 383 elements; dotted lines, 1 299 030 elements.

where y is the oxygen mass fraction in the blood; $y_{\rm i}$ is the oxygen mass fraction at the inlet; $y_{\rm w}$ is the oxygen mass fraction at the wall; n is the local normal to the vessel wall; and $D_{\rm i}$ is the vessel diameter.

2.2. *Flow conditions and waveform*

The flow waveform (figure 6) used at the inlet to modulate the fully developed profile is a three-harmonic reconstruction of the CCA waveform, given by

$$U(r,t) = \bar{U}r = 0\left[1-\left(\frac{r}{R}\right)^2\right]\left\{1 + A\left[0.5\sin\left(\frac{2\Pi t}{T}\right) + 0.45\sin\left(2\frac{2\Pi t}{T}-0.5236\right) + 0.1\sin\left(3\frac{2\Pi t}{T}+2.618\right)\right]\right\}, \qquad (2.1)$$

where $U(r,t)$ is the local axial velocity at time t; $\bar{U}_{r=0}$ is the time-averaged velocity at $r=0$; A is the amplitude factor; and T is the period. The effect of changing the pulse rate and pulsation amplitude has also been investigated, with $T\equiv[0.5,0.8,1.333]$ s, and $A\equiv[0.667, 1,1.333]$, for a total of nine flow conditions. Physiological conditions, considered here as the base case, correspond to $T=0.8$ s, $A=1$ and $\bar{U}_{r=0}=0.4\ {\rm m\ s^{-1}}$, equivalent to a time-averaged Reynolds number, $Re=\rho\bar{U}r = 0D_{\rm i}/2\mu=720$, and a Womersley number, $Wo=0.5D_{\rm i}(\omega/\upsilon)^{0.5}=4.6$, where $\omega=2\Pi/T$ is the angular frequency and $\upsilon=\mu/\rho$ is the kinematic viscosity. For the steady-state case, the velocity was set to the time-averaged condition counterpart, $\bar{U}_{r=0}=0.4\ {\rm m\ s^{-1}}$, equivalent to $Re=720$. We implemented a parabolic profile in the first instance for simplicity, but subsequently adopted a Womersley profile in the high *Wo*, high amplitude factor cases. In fact, under the present conditions, the instantaneous inlet profile is not really parabolic, although it has been used by other authors in the same range of Womersley number (Finol & Amon 2001; Mittal *et al.* 2001; Khanafer *et al.* 2006). We verified that the error associated with the use of a parabolic profile is non-relevant at $T=0.5$ s and $T=0.8$ s and $A=1.33$, for the purpose of this work. Also, the use of an analytic expression for the flow waveform does not affect the results, while it simplifies the interaction with FLUENT.

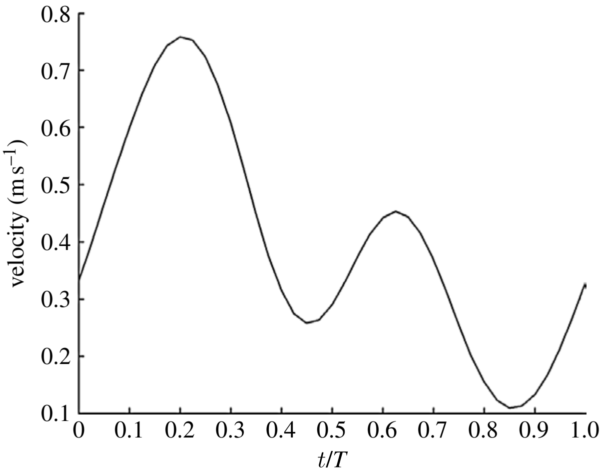

Figure 6. Three-harmonics approximation of the CCA flow waveform. Indicated is the centreline velocity.

3. RESULTS AND DISCUSSION

3.1. *Physiological conditions*

The steady-state and time-averaged iso-contours of oxygen mass fraction (figure 7) show rotation of the low-concentration area about the centre of symmetry, induced by developing helical flow causing a spiral pattern in the *Sh* number distribution (Coppola & Caro 2008). The oxygen distribution at the proximal section is not much different in the two cases, probably because the flow is not developed. The middle and distal section steady-flow contours (figure 7*a*) show a more localized area of poor oxygenation than the corresponding time-averaged ones. In the case of the time-averaged contours (figure 7*b*), the oxygen-depleted fluid is spread across a wider area. This spreading can be explained by the motion of the Dean vortices (figure 8*b*), oriented, with respect to the horizontal, at approximately −50° at $t/T=0$, at approximately 0° at $t/T=0.45$ and back at approximately −50° at $t/T=0.575$. This sweeping

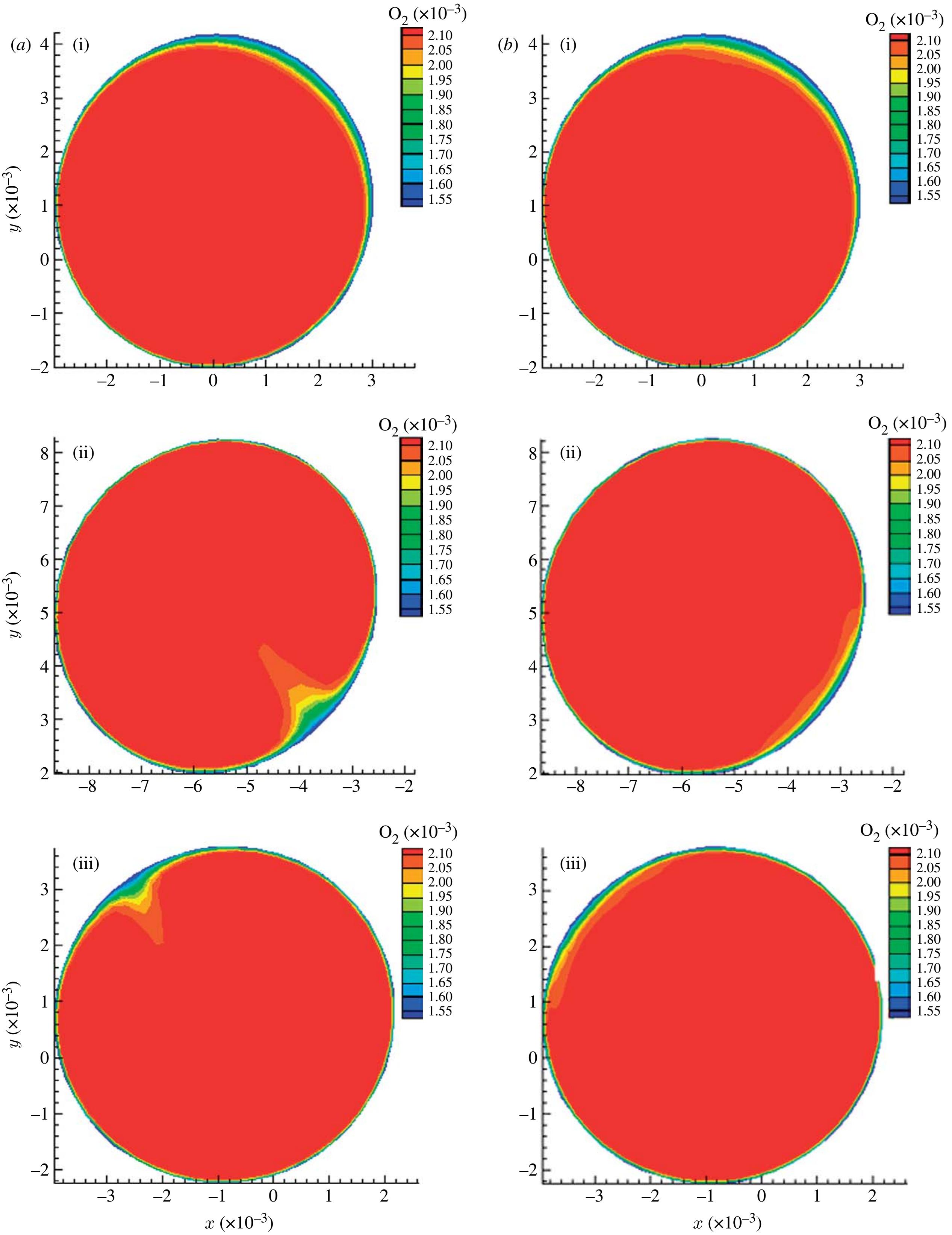

Figure 7. Oxygen iso-contours at three cross sections, for (*a*) steady and (*b*) time-averaged. (i) Proximal section, (ii) middle section, (iii) distal section.

effect is a consequence of the combination of three-dimensionality and pulsatility; it does not exist if the geometry is two-dimensional, as in a planar bend. The vortices develop, acquire strength and rotate, affecting to some extent the oxygen boundary layer (figure 8*a*), offering the oxygen-depleted fluid to a larger surface than that in the steady case. Papaharilaou *et al.* (2002) reported oscillation of the Dean vortices and WSS with pulsatile flow in an asymmetric end-to-side anastomosis.

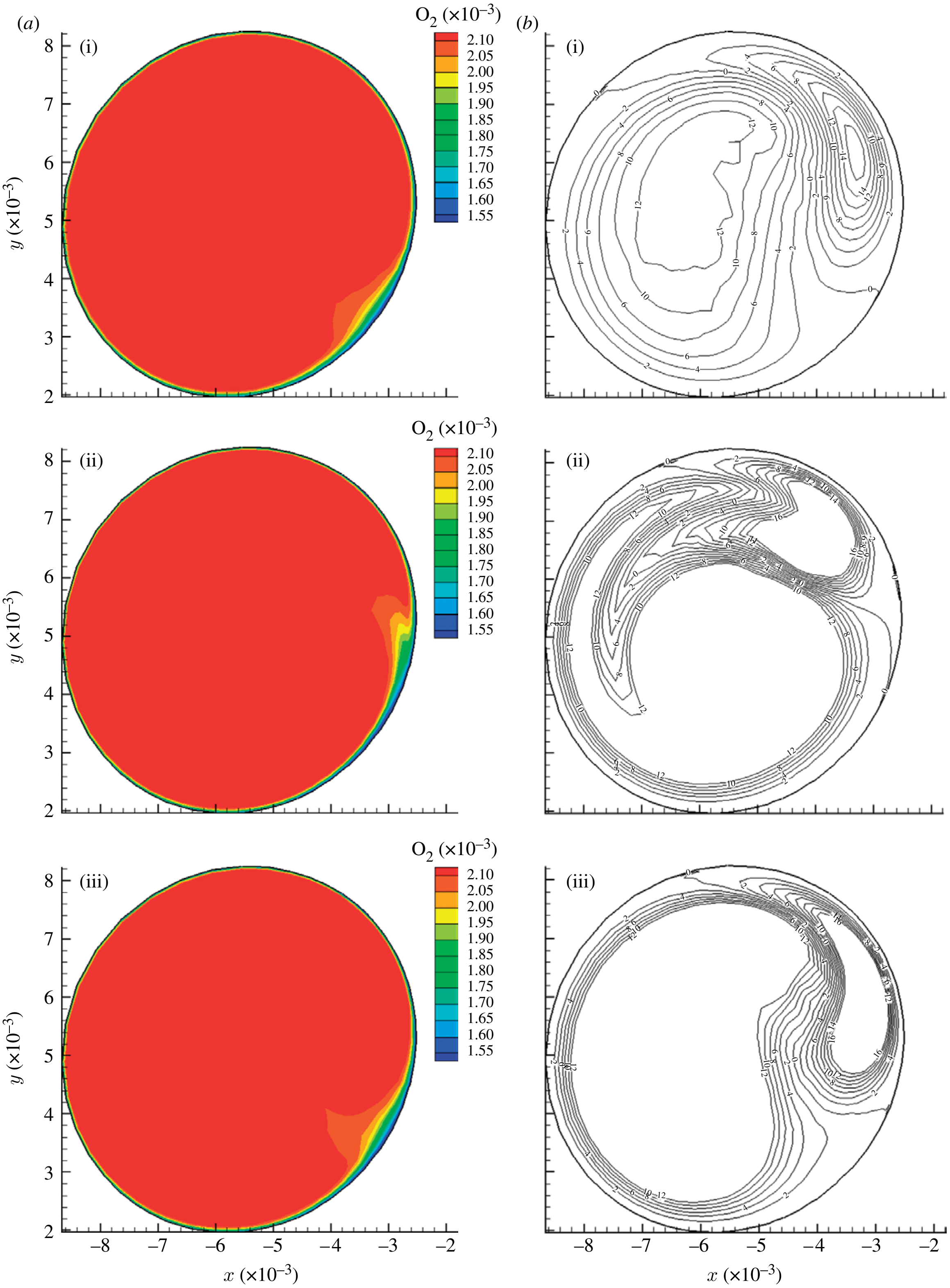

Figure 8. Oxygen mass fraction iso-contours (*a*) and corresponding helicity iso-contours (*b*) for the middle section. (i) $t/T = 0$; (ii) $t/T = 0.45$; (iii) $t/T = 0.575$.

If we now refer to the local polar coordinate system, this discussion can be translated in terms of wall quantities, by looking at the profiles of WSS and *Sh* along the circumference of each section, as measured by θ (figure 9). Here, the three horizontal dot-dashed lines represent the *Sh* value in the straight case at the same axial positions, as indicated by the colour coding. The time-averaged circumferential profiles of WSS (figure 9*a*) show that the middle and distal sections' minima are above the value of WSS (approx. 0.94 Pa) of the straight case, and at each section, the minimum WSS is anyway above 0.4 Pa, the proposed threshold value for disease development (Malek *et al.* 1999; Palumbo *et al.* 2002). In the case of the *Sh* number,

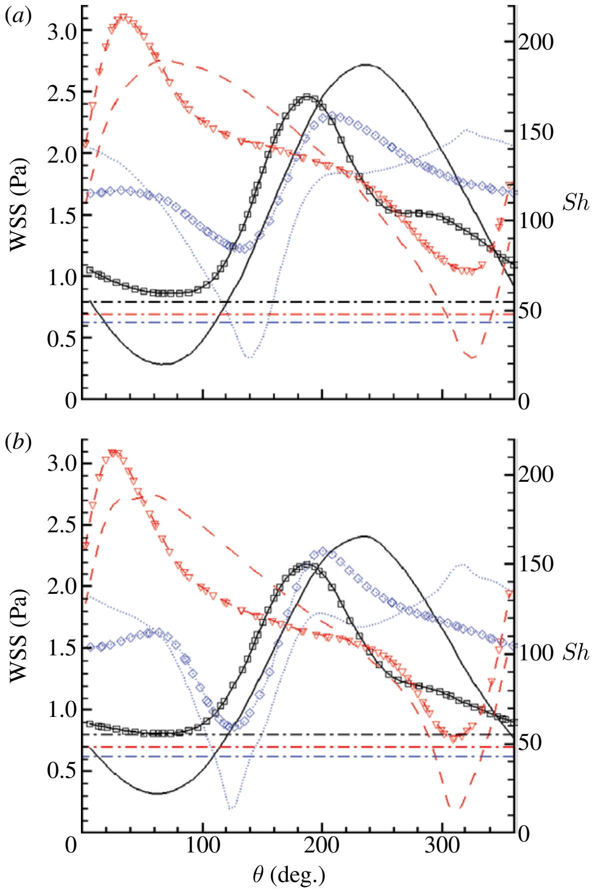

Figure 9. WSS and *Sh* profiles along the circumference of the cross sections for the steady-state case at peak velocity. Solid line, proximal section; dashed line, middle section; dotted line, distal section. Lines with symbols, WSS; plain lines: *Sh* number. The three dot-dashed lines represent the *Sh* value in the straight case at the same axial positions, as indicated by the colours. (*a*) Time-averaged state; (*b*) steady state.

approximately 100° of arc length for the proximal section and up to approximately 40° for the other sections show values lower than the corresponding straight case. Also, each of these regions appears to be shifted on average by approximately 160° with respect to the high *Sh* number region and seems to correlate with the experimental observations (figure 1). Given the ‘safe’ range of WSS and the lower localized *Sh* minima in the helical case (compared with the straight case), it could be expected that IH would be locally more developed in the helical than straight stent. We do not know why this is not so. However, it may be assumed that the deployment of a self-expanding stent in an artery causes compression of at least part of the wall, as a result of the outward-directed force of the stent acting against the elastic recoil of the vessel. Such compression could interfere with the mass transport properties of the wall (Caro & Lever 1983) and we speculate that compression of the vessel wall by the stent interferes with the mass flux at the wall, that the compression is lower at inner curvature locations in the helical geometry, and that this lower compression coupled with the higher WSS values may be counterbalancing the lower mass flux. In support of that idea is that in the outer curvature regions of the helical stent, where higher compression is expected, the development of IH is inhibited to the extent of the stent struts being covered by just a thin layer of neointima. These regions are characterized by significantly high values of *Sh* and WSS.

The steady-state profiles (figure 9*b*) show overall trends qualitatively similar to the time-averaged profiles, but with definitely lower minima. The relative differences between the time-averaged and the steady-state WSS profiles are noticeable especially at the location of the minima, with differences up to approximately 30 per cent of the time-averaged value at the middle and distal sections. At the same locations, the relative differences for the *Sh* profiles reach approximately 50 per cent of the time-averaged value. This suggests on the one hand that steady-state simulations may be sufficient to capture only the qualitative trends of WSS and *Sh* number and on the other hand that flow pulsatility may be protective against atherosclerosis and IH, at least under the conditions studied.

3.2. Effect of waveform amplitude and frequency

It was reported (Caro *et al.* 1987) that cigarette smoking, a risk factor for atherosclerosis, transiently reduces the arterial pulsatility index, $\mathrm{PI}=(U_{\max}-U_{\min})/\bar{U}$, defined as the ratio of the pulsation amplitude, $U_{\max}-U_{\min}$, and the time-averaged velocity, $\bar{U}$, at a specific point. Also, clinical evidence shows that increased heart rate may contribute to the development of atherosclerosis (Laperche *et al.* 1999; Chatzizisis & Giannoglou 2006; Himburg *et al.* 2007; Giannoglou *et al.* 2008; Hall & Palmer 2008). We speculated that alteration of the PI will alter the amplitude of the vortex oscillation and consequently we modified the waveform to evaluate its effect on the vortex motion. The pulsatility index was modified by modifying the waveform amplitude factor, A, by ±30 per cent with respect to its physiological value, $A=1$, which resulted in a $\mathrm{PI}=1.08$ at the lower amplitude, $\mathrm{PI}=1.63$ at physiological amplitude and $\mathrm{PI}=2.17$ at the larger amplitude. We also investigated the effect of pulse frequency at the different amplitudes, in the context of WSS and *Sh* number distributions, to determine the effect in the geometry under investigation. It should be pointed out that we assumed a shape-preserving waveform under the different conditions, while in reality a change in the heart rate alters the relative contribution of the diastolic phase with respect to the systolic phase (Chatzizisis & Giannoglou 2006; Giannoglou *et al.* 2008), resulting in a change in the shape of the waveform. For simplicity, only the results for the distal section are presented here. We expect the clinical results to be most repeatable at the distal section, where the flow will be more developed and less affected by entry conditions or stent deployment, and limit our discussion to this section, leaving the results for the proximal and middle sections to the electronic supplementary material. The WSS profiles shift upwards with an increasing amplitude factor (figure 10). The minimum of the *Sh* profiles (figure 10) increases as well, although to a limited extent. The effect of increasing amplitude tends to saturate as the pulsation period is increased. At a fixed period, an increase in

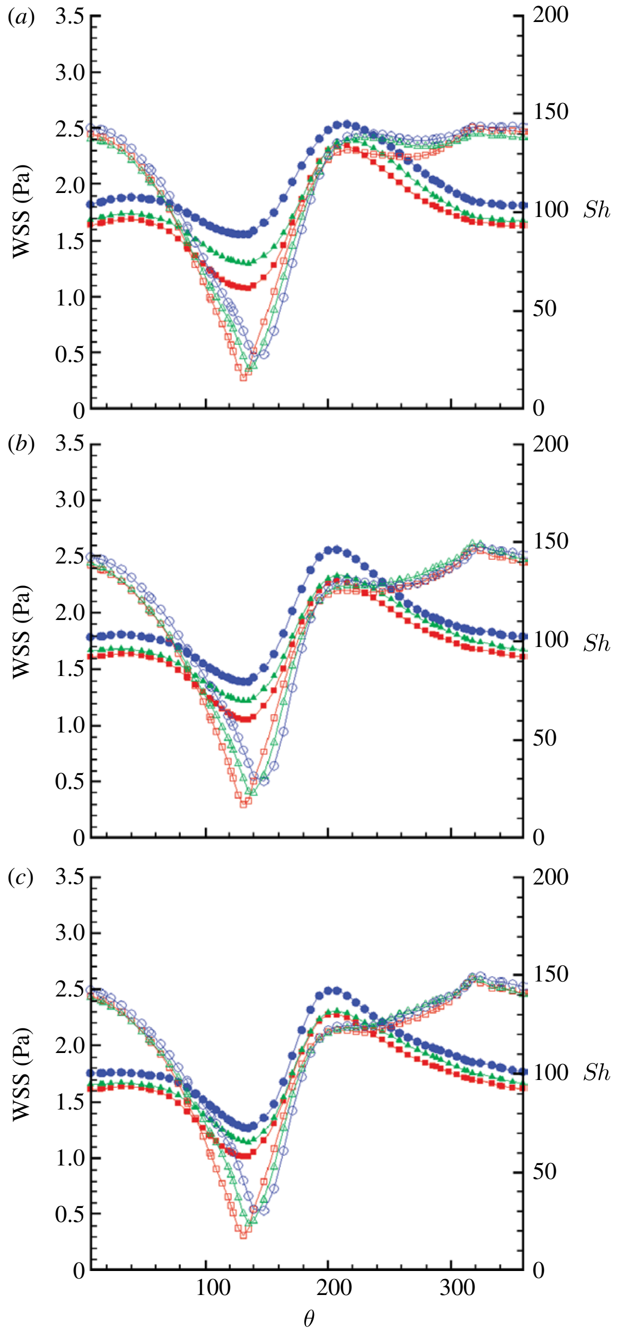

Figure 10. Time-averaged WSS (filled symbols) and *Sh* (open symbols) number profiles along the circumference of the distal section and (*a*) $T=0.5$ s, (*b*) $T=0.8$ s and (*c*) $T=1.33$ s. Squares, $A=0.66$; triangles, $A=1$; circles, $A=1.33$.

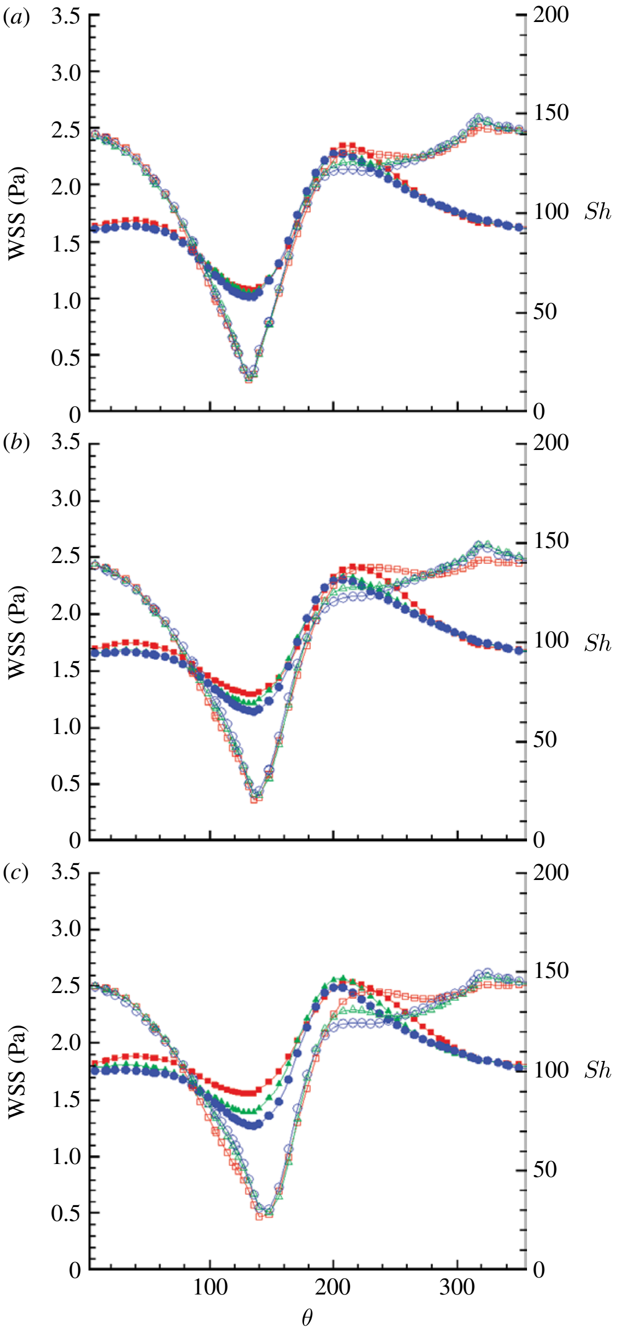

Figure 11. Time-averaged WSS (filled symbols) and *Sh* (open symbols) number profiles along the circumference of the distal section and (*a*) $A=0.66$, (*b*) $A=1$ and (*c*) $A=1.33$. Squares, $T=0.5$ s; triangles, $T=0.8$ s; circles, $T=1.33$ s.

amplitude implies steeper, positive or negative, acceleration, to accommodate larger velocity changes within the same time interval. This, in turn, will result in stronger inertia effects, enhancing flow reversal at the walls, in the decelerating phase and possible flow detachment during the accelerating phase at the inner side of the curved domain. Near-wall flow reversal conditions may explain the increasing values of WSS with amplitude, while the slight increase in *Sh* is probably a consequence of the acceleration. The saturation effect is a consequence of the lower acceleration at larger pulsation amplitude. The waveform period (figure 11) has a negligible effect on the *Sh* minima. There is also some effect on the maxima, in the sense of an upward shift with decreasing period. The WSS profiles are affected in a similar fashion, showing an upward shift with decreasing period. This upward shift is more pronounced at higher amplitude factors. At fixed amplitude, the effect of increasing the period (or decreasing the frequency) is similar to the effect of decreasing the amplitude, resulting in lower temporal velocity gradients, which are the parameters controlling the system.

We are therefore led to conclude that larger amplitude favours generally higher time-averaged WSS and *Sh*, but the effect is reduced at lower pulsation period. Also, the results suggest that higher frequency would be advantageous, by increasing WSS, in contrast to the clinically observed correlation between heart rate and atherosclerosis (Laperche *et al.* 1999; Chatzizisis & Giannoglou 2006; Himburg *et al.* 2007; Giannoglou *et al.* 2008). The contradiction between the clinical and numerical findings can possibly be explained by noting that an increase in heart rate is generally accompanied by a reduction in the duration of the diastolic phase (Chatzizisis & Giannoglou 2006; Giannoglou *et al.* 2008), not accounted for here.

4. CONCLUSIONS

A pilot study showed markedly less IH in the pig CCA after the implantation of a helical stent, as compared with a conventional stent (Shinke *et al.* 2007). A numerical study in comparable idealized models revealed that the better 'performance' of the helical stent could be partially explained by geometry-induced higher *Sh* and WSS values. In fact, the inner curvature regions of the helical model are exposed to lower oxygen flux than in the corresponding straight stent case, and yet the development of IH is lower in these regions. We are unsure concerning the explanation for this result and speculate as to its origin. It is plausible that the outward acting force, exerted by a stent against the recoil of an artery, compresses the wall compromising its mass transport properties (Caro & Lever 1983). It is plausible, moreover, that such compression and compromise of wall mass transport contribute to the occurrence of IH after stenting, and that the changes are less severe at the inner curvature regions with a helical stent than generally with a straight stent.

The IH pattern found in histological sections can only be partially described by steady flow models (steady-state simulations qualitatively capture the time-averaged WSS and *Sh* number trends) and can be related to the pulsatility-induced vortex dynamics. In particular, the sweeping motion of the vortices exposes the wall to a range of oxygen concentrations and WSS, providing, on average, higher levels of WSS and *Sh* numbers than under steady-flow conditions. These characteristics imply that vessel three-dimensionality and flow pulsatility play important protective roles in respect of IH and atherosclerosis. A sensitivity analysis suggests that large amplitude pulsation is beneficial, increasing the values of the minima in WSS and *Sh* and enhancing the 'sweeping' motion. In contrast to the clinically derived experimental evidence, higher frequencies seem to have a beneficial effect in increasing WSS minima. An increase in heart rate mainly reduces the duration of diastole, and the relative contributions of the systolic and diastolic phases should be taken into account in trying to reconcile the numerical findings and patient-derived experimental evidence.

The work was supported by the Clothworkers' Foundation, the Henry Smith Charity and the Garfield Weston Foundation.

REFERENCES

Bassiouny, H. S., White, S., Glagov, S., Choi, E., Giddens, D. P. & Zarins, C. K. 1992 Anastomotic intimal hyperplasia—mechanical injury or flow induced. *J. Vasc. Surg.* **15**, 708–717. (doi:10.1067/mva.1992.33849)

Caro, C. G. & Lever, M. J. 1983 Effect of vasoactive agents and applied stress on the albumin space of excised rabbit carotid arteries. *Atherosclerosis* **46**, 137–146. (doi:10.1016/0021-9150(83)90172-7)

Caro, C. G., Fitz-gerald, J. M. & Schroter, R. C. 1971 Atheroma and arterial wall shear observation, correlation and proposal of a shear dependent mass transfer mechanism for altherogenesis. *Proc. R. Soc. Lond. B* **177**, 109–133. (doi:10.1098/rspb.1971.0019)

Caro, C. G., Parker, K. H., Lever, M. J. & Fish, P. J. 1987 Effect of cigarette-smoking on the pattern of arterial blood-flow: possible insight into mechanisms underlying the development of arteriosclerosis. *Lancet* **330**, 11–13. (doi:10.1016/S0140-6736(87)93052-2)

Caro, C. G., Doorly, D. J., Tarnawski, M., Scott, K. T., Long, Q. & Dumoulin, C. L. 1996 Non-planar curvature and branching of arteries and non-planar-type flow. *Proc. R. Soc. Lond. A* **452**, 185–197. (doi:10.1098/rspa.1996.0011)

Caro, C. G., Watkins, N., Doorly, D. J., Sherwin, S. J. & Peiró, J. 1998 Influence of non-planar geometry on flow separation. *J. Physiol.* **513**(Pt 2), 2.

Caro, C. G., Cheshire, N., Ellis, D., Cerini, M. & Cremers, S. 2006 Implications of 3D vascular geometry. In *5th World Congress of Biomechanics, Munich, 29 July–4 August 2006*. Keynote lecture, no. 4249, p. S299.

Chatzizisis, Y. S. & Giannoglou, G. D. 2006 Pulsatile flow: a critical modulator of the natural history of atherosclerosis. *Med. Hypotheses* **67**, 338–340. (doi:10.1016/j.mehy.2006.02.005)

Coppola, G. & Caro, C. G. 2008 Oxygen mass transfer in a model three-dimensional artery. *J. R. Soc. Interface* **5**, 1067–1075. (doi:10.1098/rsif.2007.1338)

Davies, P. F. 1995 Flow-mediated endothelial mechanotransduction. *Physiol. Rev.* **75**, 519–560.

Davies, J. E. *et al.* 2007 A unifying explanation of the aortic pulse waveform in humans. *J. Am. College Cardiol.* **49**, 397A–398A.

Duda, S. H. *et al.* 2006 Drug-eluting and bare nitinol stents for the treatment of atherosclerotic lesions in the superficial femoral artery: long-term results from the SIROCCO trial. *J. Endovasc. Ther.* **13**, 701–710. (doi:10.1583/05-1704.1)

Ethier, C. R. 2002 Computational modeling of mass transfer and links to atherosclerosis. *Ann. Biomed. Eng.* **30**, 461–471. (doi:10.1114/1.1468890)

Finol, E. A. & Amon, C. H. 2001 Blood flow in abdominal aortic aneurysms: pulsatile flow hemodynamics. *J. Biomech. Eng. Trans. ASME* **123**, 474–484. (doi:10.1115/1.1395573)

Giannoglou, G. D., Chatzizsis, Y. S., Zamboulis, C., Parcharidis, G. E., Mikhailidis, D. P. & Louridas, G. E. 2008 Elevated heart rate and atherosclerosis: an overview of the pathogenetic mechanisms. *Int. J. Cardiol.* **126**, 302–312. (doi:10.1016/j.ijcard.2007.08.077)

Giddens, D. P. 1995 Fluid dynamics of end-to-side vascular grafts. In *Biological flows*. World Congress of Biomechanics Series, vol. 1. New York, NY: Plenum Publishing Corporation.

Gimbrone Jr, M. A. 1999 Vascular endothelium, hemodynamic forces, and atherogenesis. *Am. J. Pathol.* **155**, 1–5.

Hall, A. S. & Palmer, S. 2008 The heart rate hypothesis: ready to be tested. *Heart* **94**, 561–565. (doi:10.1136/hrt.2007.118760)

Himburg, H. A., Dowd, S. E. & Friedman, M. H. 2007 Frequency-dependent response of the vascular endothelium to pulsatile shear stress. *Am. J. Physiol. Heart Circ. Physiol.* **293**, H645–H653. (doi:10.1152/ajpheart.01087.2006)

Khanafer, K. M., Gadhoke, P., Berguer, R. & Bull, J. L. 2006 Modeling pulsatile flow in aortic aneurysms: effect of non-Newtonian properties of blood. *Biorheology* **43**, 661–679.

Laperche, T., Logeart, D., Cohen-Solal, A. & Gourgon, R. 1999 Potential interests of heart rate lowering drugs. *Heart* **81**, 336–341.

Lee, E. S., Bauer, G. E., Caldwell, M. P. & Santilli, S. M. 2000 Association of artery wall hypoxia and cellular proliferation at a vascular anastomosis. *J. Surg. Res.* **91**, 32–37. (doi:10.1006/jsre.2000.5891)

Lee, E. S., Caldwell, M. P., Tretinyak, A. S. & Santilli, S. M. 2001 Supplemental oxygen controls cellular proliferation and anastomotic intimal hyperplasia at a vascular graft-to-artery anastomosis in the rabbit. *J. Vasc. Surg.* **33**, 608–613. (doi:10.1067/mva.2001.113495)

Malek, A. M., Alper, S. L. & Izumo, S. 1999 Hemodynamic shear stress and its role in atherosclerosis. *J. Am. Med. Assoc.* **282**, 2035–2042. (doi:10.1001/jama.282.21.2035)

Mittal, R., Simmons, S. P. & Udaykumar, H. S. 2001 Application of large-eddy simulation to the study of pulsatile flow in a modeled arterial stenosis. *J. Biomech. Eng. Trans. ASME* **123**, 325–332. (doi:10.1115/1.1385840)

Nakazawa, G., Finn, A. V. & Virmani, R. 2007 Vascular pathology of drug-eluting stents. *Herz* **32**, 274–280. (doi:10.1007/s00059-007-2997-9)

Nichols, W. W. & O'Rourke, M. F. 1990 *McDonald's blood flow in arteries: theoretical, experimental and clinical principles*. London, UK: Edward Arnold.

Palumbo, R., Gaetano, C., Antonini, A., Pompilio, G., Bracco, E., Ronnstrand, L., Heldin, C. H. & Capogrossi, M. C. 2002 Different effects of high and low shear stress on platelet-derived growth factor isoform release by endothelial cells—consequences for smooth muscle cell migration. *Arterioscler. Thromb. Vasc. Biol.* **22**, 405–411. (doi:10.1161/hq0302.104528)

Papaharilaou, Y., Doorly, D. J. & Sherwin, S. J. 2002 The influence of out-of-plane geometry on pulsatile flow within a distal end-to-side anastomosis. *J. Biomech.* **35**, 1225–1239. (doi:10.1016/S0021-9290(02)00072-6)

Patankar, S. V. & Spalding, D. B. 1972 A calculation procedure for heat, mass and momentum transfer in three-dimensional parabolic flows. *Int. J. Heat Mass Transfer* **15**, 1787. (doi:10.1016/0017-9310(72)90054-3)

Perktold, K., Leuprecht, A., Prosi, M., Berk, T., Czerny, M., Trubel, W. & Schima, H. 2002 Fluid dynamics, wall mechanics, and oxygen transfer in peripheral bypass anastomoses. *Ann. Biomed. Eng.* **30**, 447–460. (doi:10.1114/1.1477445)

Qiu, Y. C. & Tarbell, J. M. 2000 Numerical simulation of oxygen mass transfer in a compliant curved tube model of a coronary artery. *Ann. Biomed. Eng.* **28**, 26–38. (doi:10.1114/1.251)

Shinke, T., Robinson, K. A., Gilson, P., Bruke, M. G., Cheshire, N. J. & Caro, C. G. 2007 Novel helical stent design elicits spiral blood flow pattern and inhibits neointima formation in porcine carotid arteries. *Am. J. Cardiol.* **100**, 186L. (doi:10.1016/j.amjcard.2007.09.061)

Shinke, T. *et al.* 2008 Novel helical stent design elicits swirling blood flow pattern and inhibits neointima formation in porcine carotid arteries. Poster presentation, American Heart Association meeting, New Orleans, LA, 8–12 November 2008.

Sottiurai, V. S., Yao, J. S. T., Batson, R. C., Sue, S. L., Jones, R. & Nakamura, Y. A. 1989 Distal anastomotic intimal hyperplasia: histopathologic character and biogenesis. *Ann. Vasc. Surg.* **3**, 26–33. (doi:10.1016/S0890-5096(06)62381-9)

Tarbell, J. M. 2003 Mass transport in arteries and the localization of atherosclerosis. *Annu. Rev. Biomed. Eng.* **5**, 79–118. (doi:10.1146/annurev.bioeng.5.040202.121529)

Wood, N. B., Zhao, S. Z., Zambanini, A., Jackson, M., Gedroyc, W., Thom, S. A., Hughes, A. D. & Xu, X. Y. 2006 Curvature and tortuosity of the superficial femoral artery: a possible risk factor for peripheral arterial disease. *J. Appl. Physiol.* **101**, 1412–1418. (doi:10.1152/japplphysiol.00051.2006)